Article

Ilmenite-Grafted Graphene Oxide as an Antimicrobial Coating for Fruit Peels

Piyumi Kodithuwakku, Dilushan Jayasundara,* Imalka Munaweera, Randika Jayasinghe,
Tharanga Thoradeniya, Achala Bogahawatta, K. R. Jaliya Manuda, Manjula Weerasekera,
and Nilwala Kottegoda*

Read Online

ACCESS | Metrics & More | Article Recommendations | SI Supporting Information

ABSTRACT: Postharvest loss is a significant global challenge that needs to be urgently addressed to sustain food systems. This study describes a simple microwave-assisted green synthesis method in developing a nanohybrid material combining natural ilmenite ($FeTiO_3$) and graphene oxide (GO) as a promising antimicrobial fruit peel coating to reduce postharvest loss. The natural ilmenite was calcined in an inert environment and was mixed with GO in a microwave reactor to obtain the nanohybrid. The nanohybrid was then incorporated into an alginate biopolymer to form the fruit coating. Microscopic images revealed successful grafting of $FeTiO_3$ nanoparticles onto the GO sheets. Spectroscopic measurements of Raman, X-ray photoemission, and infrared provided insights into the interactions between the two matrices. The optical band gap calculated from Tauc's relation using UV−vis data showed a significant reduction in the band gap of the hybrid compared to that of natural ilmenite. The antimicrobial activity was assessed using *Escherichia coli*, which showed a substantial decrease in colony counts. Bananas coated with the nanohybrid showed a doubling in the shelf life compared with uncoated fruits. Consistent with this, the electronic nose (E-nose) measurements and freshness indicator tests revealed less deterioration of the physicochemical properties of the coated bananas. Overall, the results show promising applications for the ilmenite-grafted GO nanohybrid as a food coating capable of minimizing food spoilage due to microbial activity.
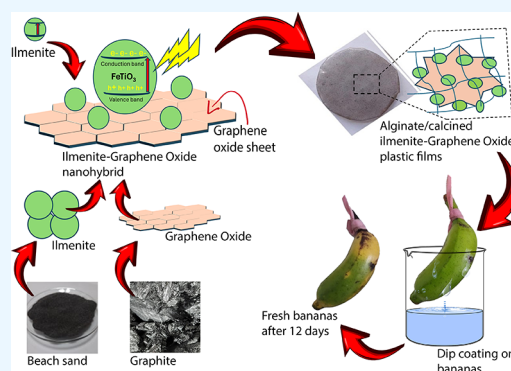
1. INTRODUCTION

Globally, postharvest loss has become one of the major problems in agricultural productivity.[1] According to the 2016 Sustainable Development Goals report, goal 2 seeks to achieve sustainable food production by 2030.[2] This is expected to be achieved by introducing sustainable agriculture, proper food market functioning, and doubling the agricultural productivity. One of the major issues pertaining to improving agricultural productivity is postharvest loss in the developing part of the world. During postharvest handling and storage, fresh food undergoes rapid deterioration leading to quality degradation and thus a substantial decrease in shelf life. Globally, conventional strategies such as cold storage, hot water treatment, gamma irradiation, controlled temperature, high humidity processes, and chemical treatments have already been used to address this issue.[3−9]

However, low efficiency, nutrient loss, safety risk, unwanted residues, and the absence of facilities to carry out some of these treatments on a commercial scale are key disadvantages of these approaches.[5,10] Therefore, advanced technologies such as nanotechnology have been explored as an alternative efficient solution in food preservation.[6,11−14]

Nanomaterials have shown progress by improving antimicrobial properties, moisture and gas barrier properties, and mechanical strength while providing biocompatibility and biodegradability for food packaging systems.[6,15−17] Functional bionanocomposite films, incorporating components such as starch, cellulose, chitosan, montmorillonite (MMT), metals, and metal oxides, have also found applications in food packaging.[18] Nanomaterials serve as reinforcements to enhance mechanical and thermal characteristics of composites, leading to the development of improved materials. Furthermore, nanomaterials facilitate the creation of active ingredients endowed with antibacterial, antioxidant, and other desirable effects. Apart from well-established options, such as silver nanoparticles and nanoclay, nanomaterials utilized in packaging comprise metal oxides, polysaccharides, proteins, halloysite nanotubes, poly(vinyl alcohol) (PVA), polylactic
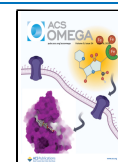
acid (PLA), polyhydroxyalkanoates (PHA), and essential oils.[18,19] These nanomaterials offer a range of functions, including antioxidant properties (e.g., essential oils, vitamins, polyphenols, and carotenoids), antibacterial effects (e.g., nanosilver, nanosilica, and nanocarbon tubes), ethylene scavenging (e.g., nano-$KMnO_4$), and oxygen scavenging (e.g., Pd nanoparticles).[18-20] Some of the nanocoatings are edible (e.g., hydroxypropylmethylcellulose (HPMC) and chitosan) and offer significant benefits such as robust mechanical properties, high consumer acceptance, and nontoxicity. However, the overall performance and cost of edible films have consistently posed challenges.[21]

Recently, metal oxide nanomaterials such as Ag_2O, TiO_2, and ZnO have received increased attention as promising antibacterial and antifungal agents due to their high efficacy.[15,22,23] In particular, the advantages of photocatalytic properties of these metal oxides have been exploited in food preservation.[13,14,24] Photocatalysis kills harmful microorganisms by releasing reactive oxygen species (ROS) such as superoxide and hydroxyl groups. These ROS damage the cell wall and DNA in microbial cells, inhibiting DNA replication and resulting in cell death. Some of the most studied metal oxides include ZnO, WO_3, CuO, and TiO_2. TiO_2, synthetic rutile, and their derivative compounds have been widely exploited as promising antimicrobial photocatalysts over the years.[25,26]

The antimicrobial property imparted by TiO_2 has been extensively studied for food packaging purposes as they are very effective against food spoilage microbes such as *Staphylococcus aureus* and *Bacillus anthracoides*.[27,28] However, due to significant thermal energy consumption during processing, such as sulfuric and chlorination procedures, its practical applications are limited. It is also a high-cost process that produces a large amount of waste. As a result, the efficacy in large-scale operations of the traditional titanium-based photocatalyst in decomposing organic contaminants remains inadequate.[29] Therefore, facile methods to develop new materials with visible-light photocatalytic activity have emerged as a unique research solution.[30-35]

Ilmenite ($FeTiO_3$) is a common natural mineral that is widely utilized to synthesize TiO_2 and synthetic rutile. It holds a lot of promise in terms of nontoxicity, chemical stability, photostability, and availability.[33,36,37] However, it has various shortcomings, such as poor visible-light absorption capacity, a wider band gap, and a high electron−hole pair recombination rate, which will limit its practical applicability and diminish the photoelectron yield. Therefore, many research has been dedicated to band gap re-engineering through structural modifications.[38-41] For this purpose, carbon-based materials of various origins, such as graphdiyne, graphitic carbon nitride, and carbon nanotubes (CNTs),[15,42] have been identified as a band gap modifier.

Graphene has a single layer of an sp^2 hexagonal honeycomb lattice and is used in nanohybrids to engineer surface functionalization. The advantages of graphene include improving electron−hole pair separation for high quantum efficiency, extending visible-light absorption for solar light harvesting, and dramatically enhancing the reactant absorbing ability for high reaction probability.[43-45] Examples of the graphene-based nanohybrids used in related applications are graphene-TiO_2, graphene-ZnO, graphene-$BiFeO_3$, GO-$FeTiO_3$, graphene-Fe_2O_3.[32,46-48]

This study describes a simple microwave-assisted green synthesis of $FeTiO_3$ derived from beach sand that has been grafted onto GO nanosheets to obtain a visible-light-active photocatalyst with a significant antimicrobial activity as a promising candidate for fruit peel coating applications to reduce postharvest loss.

2. EXPERIMENTAL SECTION

2.1. Materials and Chemicals. Analytical-grade chemicals were employed in this study without any additional purification. All of the trails used deionized water. Natural ilmenite samples were obtained from the Lanka Mineral Sand Ltd. processing plant at the Pulmoddai deposit in Sri Lanka. The chemical composition of the natural ilmenite sample is given in Table S1. Mainly natural ilmenite consists of 86.80% ilmenite, 2.90% zircon, 2.71% quartz, 2.19% garnet, and 1.40% rutile. GO used in all experiments was synthesized using Sri Lankan vein graphite according to the method reported by Nissanka et al.[49]

2.2. Isolation of $FeTiO_3$ from Beach Sand. Beach sand samples were ground using mechanochemical forces to reduce the particle sizes. The obtained product was exposed to a magnetic field of 0.5 T strength to separate ilmenite and other magnetic materials. The magnetically separated ilmenite sample was washed with distilled water using ultrasound sonication (GT Sonic-3L, 45 kHz, 30 °C, 100 W ultrasonic power) for 30 min to remove any impurities present. This washing procedure was performed four times and dried at 60 °C. Purified magnetically separated ilmenite was ground under mechanical forces to substantially reduce the particle size and calcined under an inert environment (N_2 environment) in a muffle furnace for 1 h at 350 °C to obtain the magnetically separated calcined ilmenite (cal-Ilm).

2.3. Synthesis of Calcined Ilmenite-Grafted GO Nanohybrids (Cal-Ilm/GO Nanohybrids). Cal-Ilm/GO nanohybrids were synthesized using a microwave-assisted green approach using cal-Ilm derived from beach sand and GO derived from Ceylon vein graphite. GO (10 mg) was dissolved in 5.00 mL of ethanol by sonication for 1 h to achieve uniform dispersion of GO. Next, cal-Ilm was added to the GO dispersion in a silicon carbide vessel to make 2% (w/w) GO in ilmenite, and the mixture was then heated at 140 °C for 7 min under microwave reaction conditions. Finally, the resulting cal-Ilm/GO nanohybrid was centrifuged at 7000 rpm for 5 min. The final product was washed several times with ethanol and deionized water and then dried at 60 °C.

2.4. Preparation of Food Coatings of Cal-Ilm/GO Nanohybrids. Sodium alginate, 2.5 g (the molecular weight was 216.12 g mol^{-1}, 2.5% w/v), was mixed in 50 mL of distilled water at 45 °C for 30 min until a homogeneous clear solution was obtained. Then, 1.0 g of the previously prepared cal-Ilm/GO nanohybrid was added to the polymeric mixture and stirred for 30 min to obtain a uniform suspension. Finally, a dried film of the alginate/cal-Ilm/GO nanohybrid was obtained. Control samples were prepared with alginate and alginate/cal-Ilm. The dried films were peeled off from the Petri dishes and kept in vacuum desiccators until further use.

Approximately the same weight, similarly ripened bananas belonging to the Musaceae family (Musa spp.) (also known as Seeni Kesel) of an even maturity and free of damage were obtained from Matara, Sri Lanka. The bananas were transported to the laboratory within 24 h of harvest. All the bananas were washed with distilled water and allowed to dry for 20 min.

The fruits were then coated by immersing them for 1 min into the alginate/cal-Ilm/GO nanohybrid dispersion and letting the excess coating drip out for 10 min. Control samples were prepared by coating bananas with alginate, alginate/cal-Ilm, and water only. The entire surface of bananas was evenly coated with the prepared solutions. Coated and uncoated bananas were stored at 30 °C and 40% RH under constant visible light over the storage period of 1, 6, 9, and 12 days. The experiment was triplicated.

2.5. Determination of Antimicrobial Activity.

2.5.1. Antimicrobial Activity of Cal-Ilm/GO Nanohybrids. An *Escherichia coli*-type strain (ATCC 25922) was obtained from the Department of Microbiology, Faculty of Medical Sciences, University of Sri Jayewardenepura, Sri Lanka, and was used for testing. Before the microbiological experiment, all of the glassware and samples were sterilized. On nutritional agar, stock cultures of bacteria were kept. Test strains were subcultured on Mueller−Hinton agar and incubated at 37 °C for 24 h to produce fresh microbiological cultures. A few colonies from 24 h of fresh microbial cultures were dissolved in peptone water to provide the standard inoculum for the test strain. The turbidity of the inoculum was then adjusted by comparing it to a 0.5 McFarland scale. A bacterial suspension of peptone water was prepared with the bacteria diluted to 10^{-4} by using peptone water. The concentrations of the cal-Ilm and cal-Ilm/GO nanohybrid in peptone water were 10.0 g/L. As a negative control, a different plate with only peptone water was employed. Four milliliters of the *Escherichia coli* suspension (10^{-4} dilution of 0.5 McFarland) was added to each Petri dish containing cal-Ilm and the cal-Ilm/GO nanohybrid. The samples were then placed 15 cm from light (warm white LED with the wavelength range from 400 to 700 nm) to achieve an illumination intensity of about 10,000−25,000 lux (TECPEL DLM 531), and as a control, separate samples were kept in the dark for 2 h. Each Petri dish contained 0.1 mL of the *Escherichia coli* suspension, which was used to calculate the colony forming units per milliliter (CFU/mL) for the coliform count. Each sample was replicated three times. The number of colonies obtained by plating 0.1 mL of the suspension was multiplied by the dilution factor, which was then multiplied by 10 to determine the CFU/mL. As a negative control, a different plate with only peptone water was used. All experiments were performed in triplicate. The percentage reduction was calculated as mentioned under Section 2.5.2.

2.5.2. Antimicrobial Activity of Alginate/Cal-Ilm/GO Nanohybrids. In order to find the antimicrobial activity of the films, sterile Petri dishes were coated with (A) alginate, (B) alginate/cal-Ilm, and (C) the alginate/cal-Ilm/GO nanohybrid. In a coating process, Petri dishes were coated by adding 5.00 mL of the alginate solution with 50 mg of cal-Ilm and the cal-Ilm/GO nanohybrid to the B and C Petri dishes, respectively. The contents of the Petri dishes were then dried by evaporation. Four milliliters of the *Escherichia coli* suspension was serially diluted to 10^{-4} and aseptically pipetted into each Petri dish. The inoculated Petri dishes were exposed to visible light for 2 h (50 W warm white LED with the wavelength range from 400 to 700 nm) to achieve an illumination intensity of about 10,000−25,000 lux (TECPEL DLM 531)). As a control, these samples were placed in dark conditions for 2 h. In order to obtain the *Escherichia coli* count, the *Escherichia coli* suspension was spread plated over Mueller−Hinton agar and then incubated for 24 h at 37 °C.

The percentage reduction was calculated as follows.

average reduction %

$$= \frac{\frac{CFU}{mL} \text{ in the control} - \frac{CFU}{mL} \text{ in the sample}}{\frac{CFU}{mL} \text{ in the control}} \times 100\%$$

2.5.3. Scanning Electron Microscopy Studies. Morphological changes of the *Escherichia coli* cell in the presence of cal-Ilm and cal-Ilm/GO nanohybrids left under visible light were evaluated using SEM imaging. Sterile coverslips with a 10 mm diameter (which were pretreated with concentrated sulfuric acid and 95% ethanol before the experiments) were placed at the bottom of the 12-well cell culture cluster, separately. Coverslips were then immersed in 1 mL of the prepared standardized microbial cell suspensions (0.5 McFarland) and incubated for 24 h at 37 °C. Then, the remaining cell suspensions were removed by aspiration. The coverslips were washed twice with sterilized distilled water without disturbing the surface. Then, the powder (10.0 mg/mL) in 5 mL of sterile brain heart infusion (BHI) was added dropwise onto the coverslips and kept for 2 h under visible light. After the exposure to irradiation, the coverslips were subsequently washed twice with sterile distilled water. Treated coverslips were immersed in 2.0% glutaraldehyde, and after fixing with glutaraldehyde for 24 h, samples were dehydrated in a series of ethanol solutions. Finally, the samples were air-dried overnight in an incubator followed by sputter coating with gold for 60 s. Samples were visualized under a 10k magnification using a scanning microscope (SEM; Hitachi SU 6600, Tokyo, Japan) in the secondary electron mode.

2.6. Physicochemical Properties of Nanohybrid-Coated and Uncoated Bananas.

Physicochemical properties of the alginate/cal-llm/GO nanohybrid-, alginate/cal-Ilm-, and alginate-coated and uncoated fruits as described in Section 2.4 were determined by storing bananas at constant light over the period of 1, 6, 9, and 12 days.

2.6.1. Electronic Nose Measurements. A commercial electronic nose PEN 3 (Airsense Analytics GmbH, Schwerin, Germany) was used to collect the characteristic odor of the uncoated and coated bananas. Exactly 5.0 g of banana flesh was taken and introduced to the bottles. The specifications of 10 sensors are shown in Table 1. After the initialization, sensory measurements were obtained.

2.6.2. Weight Loss Measurements. The weight loss of bananas was measured by using an analytical balance. The weight loss of bananas was calculated as a percentage of the

Table 1. Specifications of the Sensors Used in PEN3[50]

number	sensor name	general description
R1	W1C	aromatic compounds
R2	W5S	broad-range sensitivity, very sensitive to nitrogen oxide
R3	W3C	ammonia, aromatic compounds
R4	W6S	sensitive to hydrogen
R5	W5C	alkanes, aromatic compounds
R6	W1S	sensitive to methane, broad range
R7	W1W	sensitive to sulfur compounds, H₂S
R8	W2S	alcohol broad range
R9	W2W	sensitive to aromatic compounds and organic sulfur compounds
R10	W3S	reacts on high concentrations, very selective (methane)

Scheme 1. Graphical Illustration of the Synthesis of the cal-Ilm/GO Nanohybrid and Its Application as an Antimicrobial Agent and Food Preservative Material
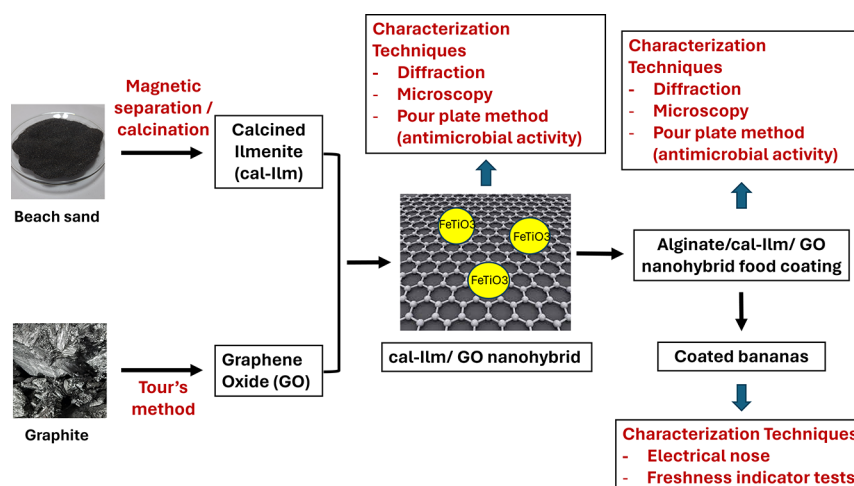
weight loss after storage compared to the initial weight by weighing the initial banana samples before and after storage. The following equation was used to calculate the weight loss percentage, when w_0 is the initial weight while w_t is the weight in the storage time period.

$$\text{weight loss \%} = \frac{W_0 - W_t}{W_0} \times 100\%$$

2.6.3. Firmness Analysis. The firmness of the bananas was measured with a penetrometer mounted on a tested stand using a 7 mm-diameter cylindrical probe.[51] Firmness was defined as the maximum punch force (N) required until tissue failure occured, and measurements were taken at the middle part from the stem end and distal end of the banana. The firmness measurements were replicated five times for each treatment.

2.7. Statistical Analysis. Data were analyzed using Origin Pro 9.0 64 commercial software. The significant difference between the variables was tested by using a one-way ANOVA with a 95% level of significance (P, 0.05).

2.8. Characterization. An X-ray diffractometer (Rigaku Ultima IV, Japan) with a scintillation counter detector was used to obtain powder X-ray diffraction (PXRD) data. The diffractometer was operated with a Cu Kα X-ray source (λ = 1.141 Å) at a current of 30 mA and a voltage of 40 kV. PXRD patterns were collected at the 2θ range of 5–80° with a scan speed of 2 deg min^{-1} and a 0.02° step size. The obtained patterns were analyzed by using PDXL2 software. In order to identify the functional groups, Fourier transform infrared spectra (FTIR) were obtained using a Bruker Vertex 80, at the ATR mode with a ZnSe crystal and 128 scans at a 4 cm^{-1} spectral resolution. All spectra were recorded over the range from 4000 to 500 cm^{-1}. A Thermo Scientific ESCALAB Xi+ instrument was used to collect X-ray photoelectron spectroscopy (XPS) measurements of beach sand and cal-Ilm and the cal-Ilm/GO nanohybrid. Samples for XPS analysis were prepared by affixing hard pellets to the surface of conducting Cu (3M) tape. The X-ray source was a monochromatic Al Kα source. The intensity of the spectra was standardized to the number of scans, and the binding energy scale was aligned to adventitious carbon at 284.5 eV. Raman spectra were collected using a Thermo Scientific DXR 2 Raman spectrometer. Diffuse

reflectance spectroscopy (DRS) data were obtained by using a LAMBDA 365 spectrophotometer to calculate the band gap energy. The surface morphology of the nanohybrid was determined using scanning electron microscopy (SEM) (Carl Zeiss EVO 18 Research), and elemental mapping was collected using an EDAX analyzer at a 20 kV accelerating voltage. Transmission electron microscopy (TEM) analysis was performed at 200 kV using a JEOL JEM 2100 microscope. The sample was ultrasonically dissolved in methanol for 5 min before being loaded onto lacey carbon-coated copper grids (300 mesh). The sample-containing grids were dried for 24 h prior to observation.

3. RESULTS AND DISCUSSION

This investigation underscores the application of hybrid photocatalysts comprising natural ilmenite and GO for the mitigation of postharvest losses. Here, the nanohybrid is synthesized using microwave-assisted methods based on green principles, where we utilized the available natural doping of TiO$_2$. The modification process is explained in Scheme 1. The structure−property relationship is investigated using spectroscopic and microscopic techniques, while microbial and food quality was investigated using model food pathogens and electronic nose measurements. The structural and chemical characterizations of natural ilmenite, cal-Ilm, and ca-Ilm/GO were carried out using PXRD, Raman, FTIR, and XPS techniques.

3.1. Characterization of Natural Ilmenite, Cal-Ilm, and the Cal-Ilm/GO Nanohybrid. Magnetic separation is widely used in the mineral sand industry to recover titanium-bearing minerals like ilmenite from heavy mineral concentrates.[52] In this research, titanium-bearing ilmenite mineral was recovered from beach sand using a magnetic separator followed by special processing techniques to reduce the particle size and to obtain FeTiO$_3$. To prepare a cal-Ilm/GO nanohybrid, a suspension of GO was prepared. The strong hydrophilic nature of oxygen functionalities in GO sheets makes it readily soluble in an aqueous medium. The homogeneous colloidal suspension of exfoliated GO in an aqueous medium is dark brown color. Cal-Ilm nanoparticles were incorporated with an exfoliated GO to get the cal-Ilm/GO nanohybrid in a microwave reactor. The
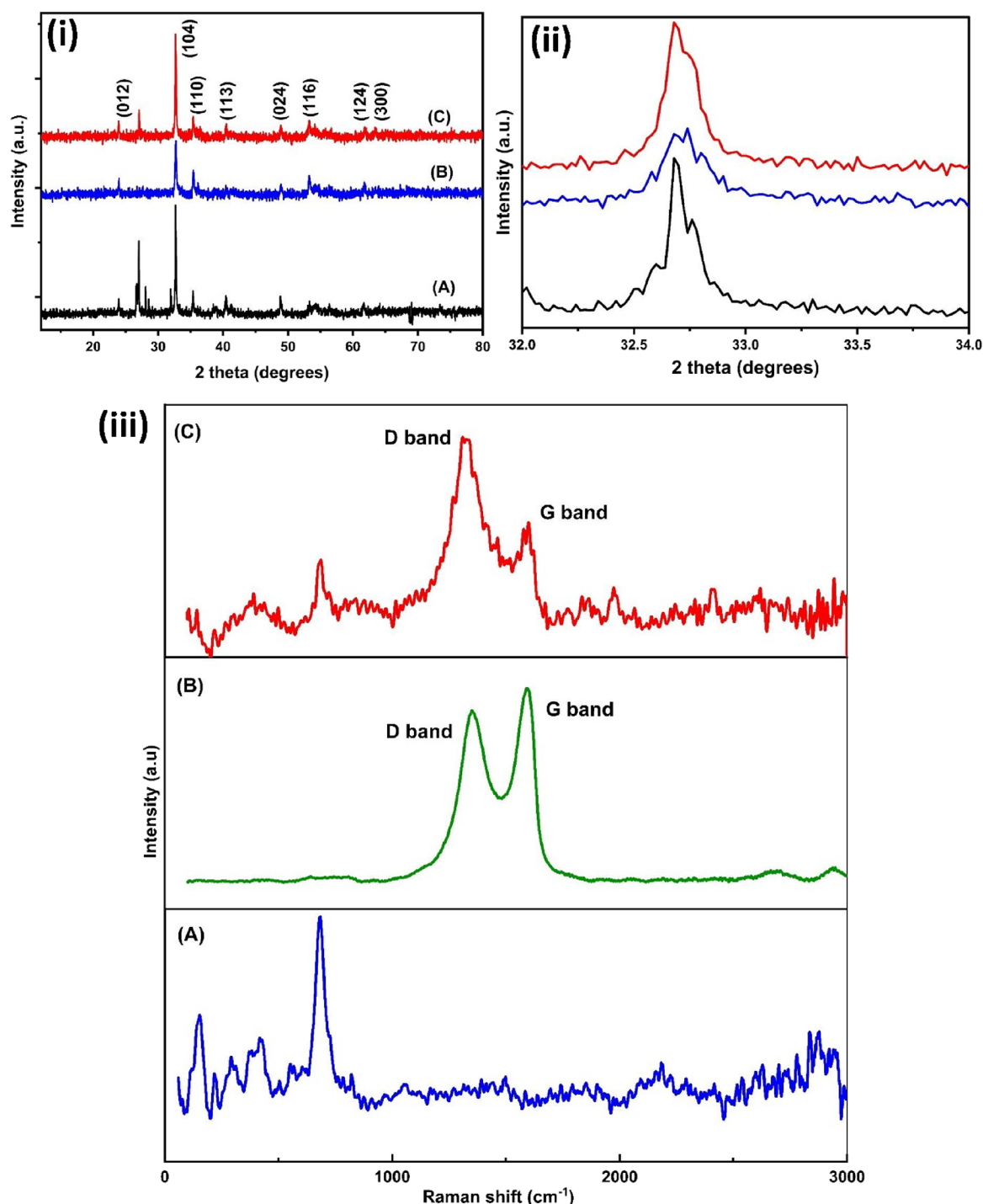
Figure 1. (i) PXRD patterns of (A) natural ilmenite, (B) cal-Ilm, and (C) the cal-Ilm/GO nanohybrid. (ii) Enlarged 32−34° region of the same PXRD patterns in the same order. (iii) Raman spectra of (A) cal-Ilm, (B) GO, and (C) the cal-Ilm/GO nanohybrid

structural features of the nanohybrid were evaluated to understand its properties toward antimicrobial behavior.

Figure 1(i) summarizes the PXRD results, which enabled us to identify the phases in the natural ilmenite, cal-Ilm, and cal-Ilm/GO nanohybrid. The PXRD pattern of natural ilmenite exhibits high-intensity peaks that correspond to the characteristic patterns of ilmenite (iron titanate ($FeTiO_3$)) (JCPDS PDF no. 01-070-6246), quartz (SiO_2) (JCPDS PDF no. 01-070-3755), and zircon ($ZrSiO_4$) (JCPDS PDF no. 01-081-0591). The PXRD peak positions for the cal-Ilm are located at ~23.9 (012), 32.7 (104), 35.4 (110), 48.2 (024), 54.0 (116),

61.6 (124), and 63.4° (300), corresponding to the characteristic pattern of the iron titanate ($FeTiO_3$) (JCPDS PDF no. 01-070-6246) phase, where the 32.7° (104) peak was the most intense XRD peak in cal-Ilm. According to the crystallographic data, $FeTiO_3$ in natural ilmenite has a rhombohedral crystalline form.[53] However, there are no detectable peaks for SiO_2 and $ZrSiO_4$ in cal-Ilm, which demonstrates the presence of $FeTiO_3$ as the major crystalline phase. The PXRD pattern of the cal-Ilm/GO nanohybrid also shows the main diffraction peak for $FeTiO_3$, suggesting the presence of the $FeTiO_3$ phase as the major phase. It could be observed that GO, having a single

PXRD peak at 9.5°, disappeared in the prepared cal-Ilm/GO nanohybrid, which might be due to the small percentage of GO (2 wt %) in the final nanohybrid. The (104) peak at 32.69° for the cal-Ilm/GO nanohybrid is much broader than that of natural ilmenite and cal-Ilm as shown in Figure 1(ii). The peak broadening indicates that the lattice structure of cal-Ilm is slightly distorted by the interaction with the GO under microwave reaction conditions.[54] Furthermore, the broad nature of the ilmenite peak implies that the particles in the cal-Ilm/GO nanohybrid are relatively small in size compared with the particles in the natural ilmenite and cal-Ilm. The average crystallite sizes of the ilmenite nanoparticles in the cal-Ilm/GO nanohybrid are in the range of 40−60 nm, which is smaller than natural ilmenite (20−100 nm) and calculated using the Scherrer equation based on the PXRD peak broadening of the (104) peak.

The structural modifications after GO incorporation are interpreted using Raman data. The positions and widths of Raman bands in materials are well-known to be related to their vibrational and structural properties. Figure 1(iii) shows the Raman spectra of the cal-Ilm, GO, and cal-Ilm/GO nanohybrid. The Raman-active modes are predicted and assigned based on ionic vibrations. A_g (1) and E_g (1) vibrational modes are assigned to Ti−O stretching motions, while the A_g (2), A_g (3), E_g (2), and E_g (3) vibrational modes are assigned to the O−Ti−O bending motions. A_g (1) and E_g (1) vibrational modes are assigned to Ti−O stretching motions, while A_g (2), A_g (3), E_g (2), and E_g (3) vibrational modes are assigned to O−Ti−O bending motions. The TiO_6 octahedral translations against Fe^{2+} cations are represented by A_g (4) and E_g (4) modes, and the Fe^{2+} cation translations against the oxygen framework are represented by E_g (5).[55] Distribution modes centered around 152, 275, 342, 392, 470, 592, and 695 cm^{-1} correspond to E_g (5), A_g (4), E_g (3), A_g (3), E_g (2), E_g (1), and A_g (1) modes, respectively, in the cal-Ilm (Figure 1(iii) A), confirming the presence of the ilmenite phase. The major peak at around 698 cm^{-1} is attributed to the Ti−O stretching mode. In the cal-Ilm/GO nanohybrid, a Raman band centered at 698 cm^{-1} was shifted to 672 cm^{-1}. This may be due to the change of the Ti−O stretching mode with the incorporation of GO under microwave conditions.

Raman spectroscopy further provides evidence of the successful incorporation of GO into the lattice of cal-Ilm. Raman band intensity shifts and changes in positions give insight into the nature of carbon−carbon bonds and defects. According to Figure 1(iii) B, the characteristic D band and G band were observed in both GO and the cal-Ilm/GO nanohybrid (see Table 2). The G band provides information

Table 2. D and G Band Positions in the Prepared Samples

material	D band (cm^{-1})	G band (cm^{-1})
Cal-Ilm/GO nanohybrid	1337	1599
GO	1326	1605

on in-plane vibrations of sp^2 bonded carbons, while the D band is a common feature for sp^3 defects in carbon.[54,56,57] The D band and G band in the cal-Ilm/GO nanohybrid were found to be shifted from their emblematic positions compared to the band positions in GO as shown in Table 2. Such shifts happen due to the incorporation/immobilization of ilmenite particles onto the GO. It shows obvious differences in D bands, which are at 1326 and 1337 cm^{-1} in GO and the cal-Ilm/GO

nanohybrid, respectively. The D band shows a higher wavenumber shift, suggesting a change in sp^3 bonds. The hump of the D band shows a blueshift due to the stress induced by ilmenite particles anchored on the surface of GO, thus increasing the sp^3 electron density. However, the intensity ratio of D:G bands of GO increases from 0.88 to 1.94 in the cal-Ilm/GO nanohybrid, suggesting a decrease in the size of the in-plane sp^2 domains and a partial ordering in the crystal structure of the ilmenite.

Figure 2 shows the typical microscopic (SEM and TEM) images of the natural ilmenite, cal-Ilm, and the cal-Ilm/GO nanohybrid. SEM images of natural ilmenite (Figure 2(i)) clearly show the disorganized macro nature of the natural ilmenite particles, which are in the nonuniform size. The particle size of natural ilmenite varies from ∼60 up to ∼260 μm. That of the cal-Ilm nanoparticles (see Figure 2(ii)) is in the range of 70−850 nm, and most of them are irregular in shape. Compared to Figure 2(ii), SEM analysis of the cal-Ilm/GO nanohybrid shows that the ilmenite particles are grafted onto the GO sheet during the microwave reaction process. Figure 2(iii) clearly exhibits that the sheet morphology of the GO sheet is retained even after the microwave treatment, and ilmenite particles are distributed on the GO sheet. The elemental analysis of the natural ilmenite, cal-Ilm, and cal-Ilm/GO nanohybrid was carried out using energy-dispersive (EDX) spectra of the samples (Figures S1, S2, and S3 in the Supporting Information). All three EDX spectra of SEM show peaks corresponding to iron (Fe) and titanium (Ti), while the EDX results for the cal-Ilm/GO nanohybrid indicate the presence of carbon (C), oxygen (O), titanium (Ti), and iron (Fe). Therefore, the high-intensity C peak in the cal-Ilm/GO nanohybrid should be attributed to the existence of GO in the prepared nanohybrid, and SEM analysis further confirms the formation of the cal-Ilm/GO nanohybrid during the microwave reaction process.

The external morphology and microstructure of the nanohybrid were studied by TEM. The semitranslucent GO nanostructure can be observed owing to its ultrathin sheetlike nature (see Figure 2(iv)). As for the cal-Ilm/GO nanohybrid, the ilmenite nanoparticles are on the GO sheet as shown in Figure 2(v). In addition, the edges of the GO can also be observed. This suggests that the GO acts as a matrix for the cal-Ilm nanoparticles. The high-resolution TEM (HRTEM) image (see Figure 2(vii)) of the cal-Ilm/GO nanohybrid showed clear lattice fringes, which allowed for the identification of the crystallographic spacing and showed a proper interface between cal-Ilm particles and GO. In addition, it reveals that the cal-Ilm nanoparticles are grafted onto the dense layer of GO (104), while the cal-Ilm particles are well-crystallized with the interlayer distances of 0.2755 and 0.2545 nm and can be assigned to the (104) and (110) plane directions, respectively. These outcomes are relatively consistent with the interlayer distances estimated from the positions of the PXRD peaks. The corresponding SAED pattern (see Figure S4) of the cal-Ilm/GO nanohybrid presents a ring diffraction pattern and discloses its polycrystalline feature, which is also consistent with the PXRD results.

X-ray photoelectron spectroscopy (XPS) was used to further examine the chemical state of the cal-Ilm/GO nanohybrid. The survey spectra confirm the presence of Fe 2p, Ti 2p, O 1s, and C 1s in the cal-Ilm/GO ilmenite nanohybrid (Figure S5). The high-resolution spectrum of Fe 2p is shown in Figure 3(i). The peaks at 712.38, 712.20, and 712.31 eV correspond to the Fe
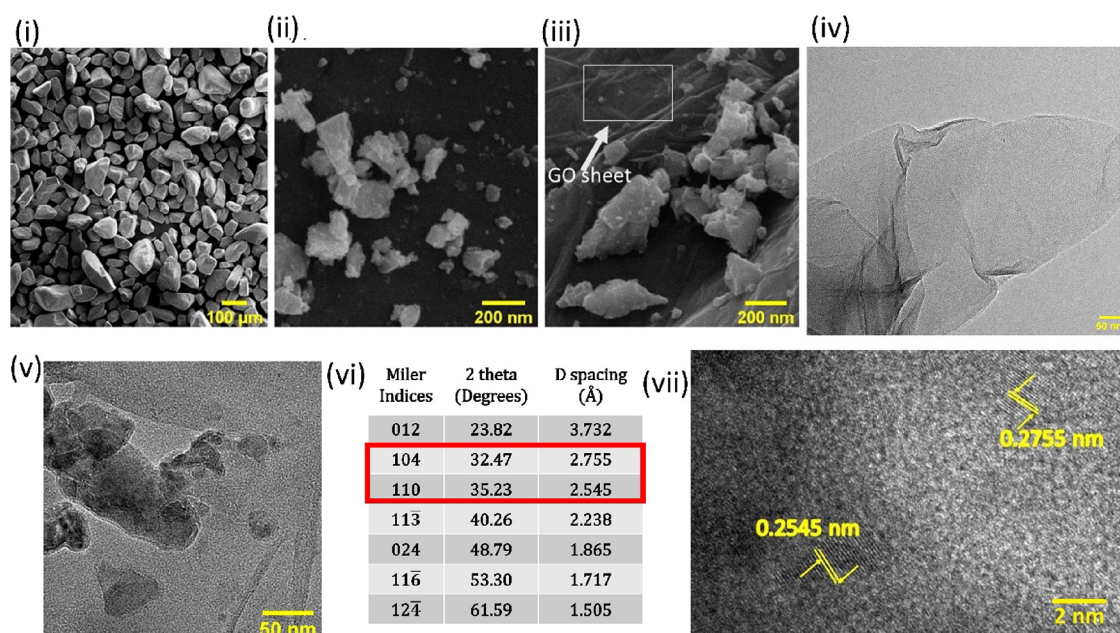
Figure 2. SEM images of (i) natural ilmenite, (ii) cal-Ilm, and (iii) the cal-Ilm/GO nanohybrid (the inset shows the GO sheet present in the cal-Ilm/GO nanohybrid); TEM image of (iv) GO; (v) high-resolution TEM image of the cal-Ilm/GO nanohybrid; (vi) Miller indices, 2 theta values, and *d*-spacing of the cal-Ilm/GO nanohybrid; (vii) high-resolution TEM image of the cal-Ilm/GO nanohybrid showing the interlayer distances.
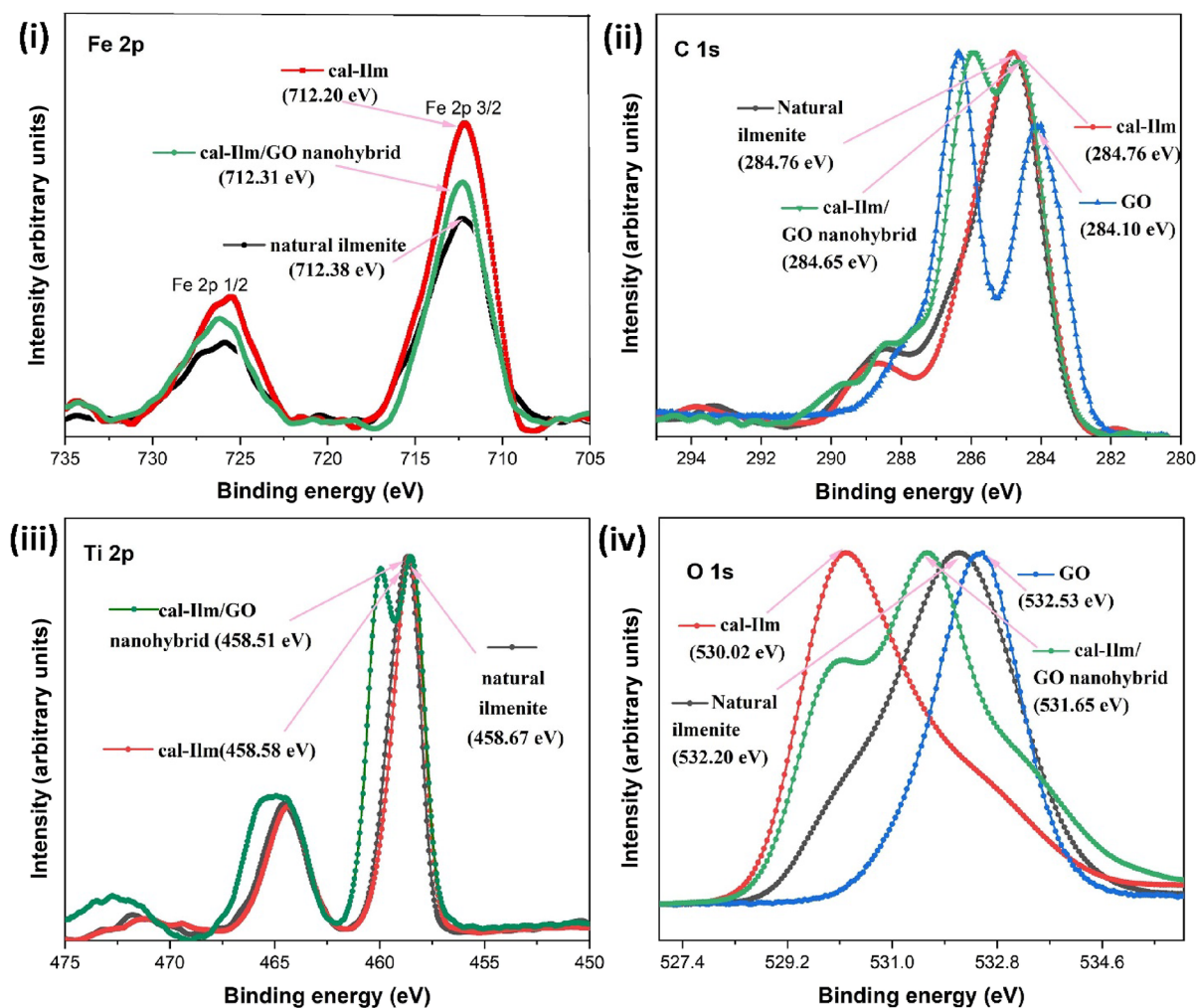

Figure 3. High-resolution XPS spectra of (i) Fe 2p, (ii) C 1s, (iii) Ti 2p, and (iv) O 1s.

$2p_{3/2}$ of natural ilmenite, cal-Ilm, and cal-Ilm/GO, respectively. The positive shift $(0.11\ eV)$ in the binding energy of the cal-Ilm/GO nanohybrid, compared to that of cal-Ilm, may have happened due to the change of the chemical environment in which Fe exists. The incorporation of GO with cal-Ilm under microwave reaction conditions might be the reason for such a chemical environment change. The binding energies for C 1s (see Figure 3(ii)) in natural ilmenite and cal-ilm have a similar binding energy value of 284.76 eV, and GO shows two significant peaks for C 1s at 284.10 and 286.37 eV. The incorporation of GO into Ca-Ilm is evident from the change in the peak shape observed in cal-Ilm/GO. Furthermore, this also indicates the significant interaction between the two components in the nanohybrid.

In addition, the data in Figure 3(iii) show two significant peaks corresponding to Ti $2p_{3/2}$ and Ti $2p_{1/2}$. The peak positions at 458.67, 458.58, and 458.51 eV correspond to the Ti $2p_{3/2}$ of natural ilmenite, cal-Ilm, and the cal-Ilm/GO nanonybrid, respectively. A slight shift can be observed in Ti compared to the shift of Fe 2p and C 1s. In addition, the binding energy shift and the change in the peak shape of O 1s (see Figure 3(iv)) in the cal-Ilm/GO nanohybrid also confirm the change of the chemical environment around cal-Ilm after the incorporation with GO. All these findings imply the significant interaction between the cal-Ilm/GO nanohybrid where the electron transformation takes place. It is feasible to draw the conclusion from the explanation above that the synthesis of the cal-Ilm/GO nanohybrid by the microwave-aided technique connects cal-Ilm and GO more intimately while keeping ilmenite particles on the GO sheet.

The diffuse reflectance spectra were used to calculate the band gaps of the materials. The $[F(R)h\nu^2]$ plot for direct transition was obtained according to the Kubelka−Munk function, $F(R)$, which is equivalent to the absorbance of the material in the UV−vis spectrum; $h\nu = (1239/\lambda)$ eV, where λ is the wavelength in nm. The value of $h\nu$ is extrapolated to $F(R)h\nu = 0$, which gives the absorption energy corresponding to the band gap E_v.[58] The band gap energy values obtained for natural ilmenite, cal-Ilm, and the cal-Ilm/GO nanohybrid were 3.37, 2.90, and 2.63 eV, respectively. This means that the photocatalytic activity may exist in the visible-light region. Also, it is to be noted that the band gap value in $FeTiO_3$ is lower than the one corresponding to pure titanium dioxide due to the presence of iron, which introduces additional electronic states and decreases the band gap.[59] Ilmenite embedded on the GO layer plays a critical role in harvesting visible-light energy, which is expected to enhance its full-light-driven photocatalytic activity.

Fingerprint regions of the FTIR spectra of natural ilmenite, cal-Ilm, and cal-Ilm/GO nanohybrids are shown in Figure 4. The peaks located at $400-800\ cm^{-1}$ belong to Ti−O−Ti and Fe−O bonds. The bands at $\sim450\ cm^{-1}$ are related to Fe−O vibrations. Interestingly, when ilmenite combined with GO, a shift in the Ti−O−Ti/Fe−O region vibration was observed, indicating a favorable interaction between the cal-Ilm and the GO matrix. Furthermore, a blueshift in the FTIR spectra of the Fe−O region, of the cal-Ilm/GO nanohybrid compared to the cal-Ilm, suggests that the interaction of the GO with cal-Ilm leads to changes in the electron density around the Fe−O functional group. Interestingly, when cal-Ilm combined with GO, a shift in the corresponding values of 420 (natural ilmenite) to $438\ cm^{-1}$ (cal-Ilm/GO nanohybrid) was
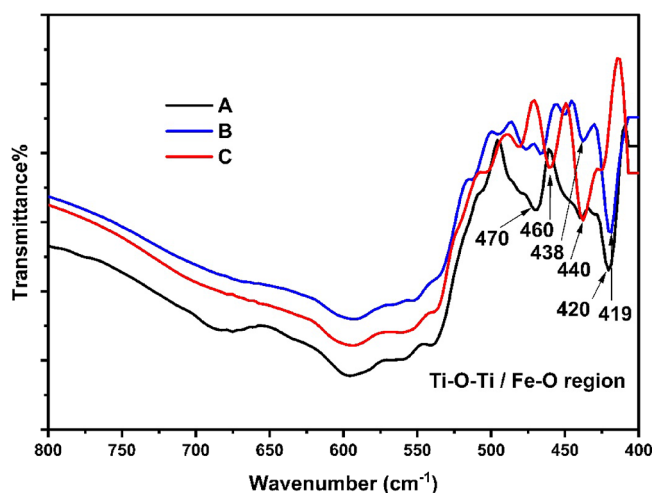
Figure 4. Fingerprint regions of the FTIR spectra of (A) natural ilmenite, (B) cal-Ilm, and (C) the cal-Ilm/GO nanohybrid.

observed, indicating a better interaction between ilmenite particles and GO.

To produce a food coating, the nanohybrid was further mixed with a biomaterial, alginate. The photographs of pure alginate, alginate/cal-Ilm, and alginate/cal-Ilm/GO nanohybrid films are presented in Figure 5. The antimicrobial activity and the food preservation ability of the cal-Ilm/GO nanohybrid were tested, and their results are discussed in the next section.

3.2. Antimicrobial Activity of the Cal-Ilm/GO Nanohybrids. Scanning electron microscopy was used to observe the cell structure of *Escherichia coli* before and after treatment with the nanohybrids. The morphological changes of *Escherichia coli* cells treated with the cal-Ilm and cal-Ilm/GO nanohybrid compared to the control are shown in Figure 6. SEM images of *Escherichia coli* (Figure 6(i)) before treatment with the nanohybrid showed that the untreated bacteria were rod-shaped, with smooth and intact cell walls. These data confirm that *Escherichia coli* cell membranes were intact before treatment with the nanohybrids, in agreement with the above results. After 2 h of light treatment of *Escherichia coli* with cal-Ilm and the cal-Ilm/GO nanohybrid, the cell walls of *Escherichia coli* became significantly damaged and slowed, and the cell size and shape were changed with cell wall abnormalities and leakages of intracellular components. Most importantly, it was noticed that the *Escherichia coli* population reduced with the nanohybrid. In the low-resolution images of *Escherichia coli* (20 μm), a large number of *Escherichia coli* population can be observed, and it has reduced for some extent compared to the cal-Ilm, while there is a significant reduction with the cal-Ilm/GO nanohybrid (note: in Figure 6(iii), the small particles are cal-Ilm particles and not the *Escherichia coli*). The strong adhesion of the cal-Ilm/GO nanohybrid to the bacteria may result in the destruction of the cell membranes (see Figure 6(ii,iii)) accompanied by cell deformation and a change in cells.

Since SEM imaging is a qualitative method, to compare the antibacterial activities accurately, the colony forming count method was used to evaluate the antibacterial activity of the cal-Ilm and cal-Ilm/GO nanohybrid. As shown in Figure 7, the CFU of *Escherichia coli* reduced after 2 h in the presence of both cal-Ilm and the cal-Ilm/GO nanohybrid following visible-light exposure compared to the control having only *Escherichia coli* with peptone water exposed to visible light. There was no
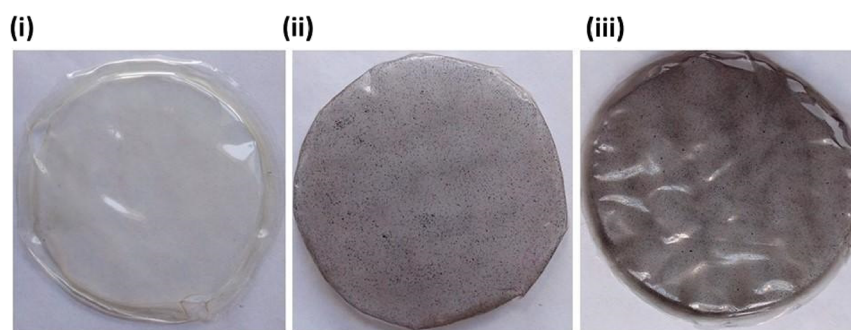
Figure 5. Photographs of the (i) alginate film, (ii) alginate/cal-Ilm film, and (ii) alginate/cal-Ilm/GO nanohybrid.
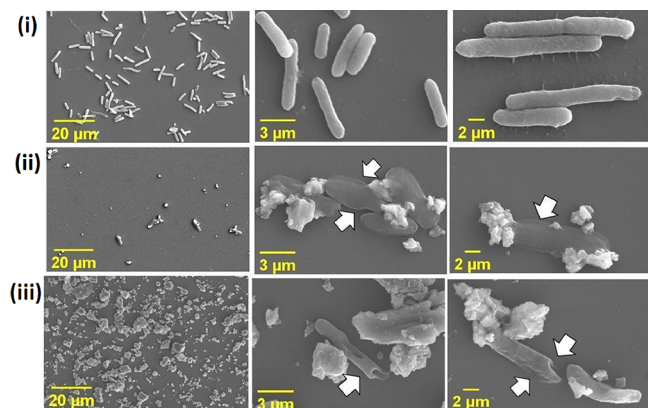

Figure 6. SEM images showing the effect of the *Escherichia coli* sample after 2 h of irradiation with (i) the control having only *Escherichia coli* with peptone water, (ii) a sample having *Escherichia coli* with peptone water and cal-Ilm, and (iii) a sample having *Escherichia coli* with peptone water and the cal-Ilm/GO nanohybrid.

cal-Ilm/GO nanohybrid, respectively. The antimicrobial activity of the cal-Ilm/GO nanohybrid showed a significant reduction in colony forming units. Figure 7(ii) shows the antibacterial activity of the alginate/cal-Ilm and alginate/cal-Ilm/GO nanohybrid films. These results are also consistent with those obtained with the powder forms of the samples. Therefore, both powder and film forms of samples display antimicrobial activity against *Escherichia coli* under visible-light illumination. However, the antimicrobial activity of the powder form is higher compared to the films prepared by incorporating the materials. This may be due to the better interaction of ilmenite particles with microorganisms compared to that of the film form.

There are several potential mechanisms in ilmenite material to show its antimicrobial effect. Nurdin et al. have reported the antimicrobial activity of synthetic ilmenite under visible-light conditions.[60] Generally, the surface of microorganisms carries a negative charge, and it reacts with particles with positive charges, resulting in an electromagnetic attraction between microorganisms and the particles, which leads to an oxidation reaction. Sun and Wu have reported the antibacterial mechanism of Fe^{3+} against bacteria. According to the study, the bacteria could adsorb Fe^{3+} and reduce this metal.[61] Iron is a nutritionally essential trace element that has a function in metabolism. However, it has significant bacteriostatic effects. Iron is a devastating metal and reacts with hydrogen peroxide
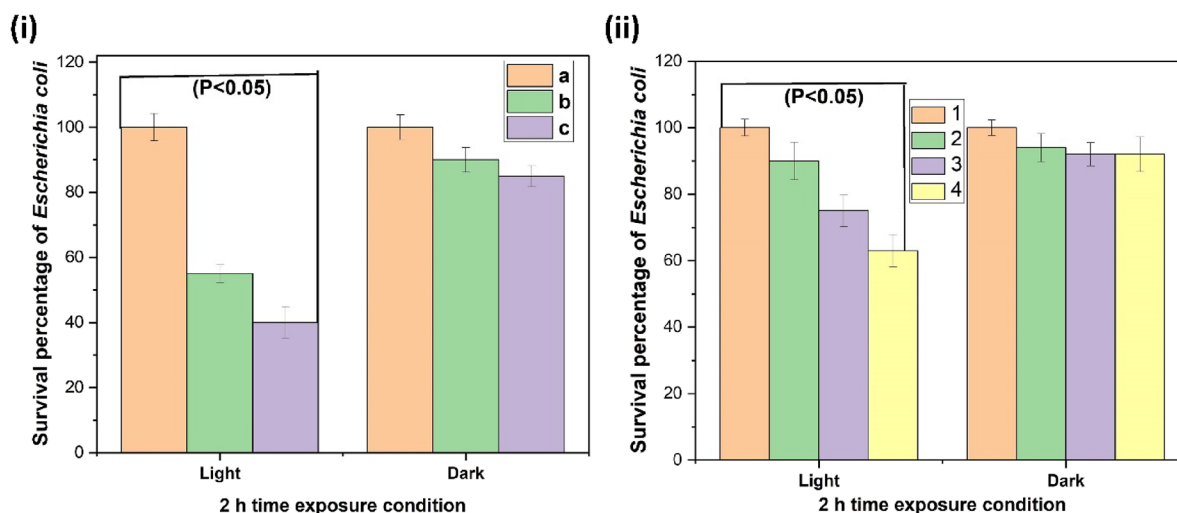
significant reduction in CFU with these samples under dark conditions. Therefore, the CFU of bacteria showed that cal-Ilm and the cal-Ilm/GO nanohybrid have antibacterial effects. The average percentage reduction of *Escherichia coli* was seen to be approximately 45 and 60% by treatment with cal-Ilm and the

Figure 7. Survival percentage of *Escherichia coli* in dark and light conditions. (i) (a) Control having only *Escherichia coli* with peptone water and (b) control having *Escherichia coli* with peptone water and cal-Ilm and (c) with cal-Ilm/GO nanohybrid; (ii) (1) control having *Escherichia coli* with peptone water and (2) alginate film, (3) alginate/cal-Ilm film, and (4) alginate/cal-Ilm/GO nanohybrid film. Each column represents means ± standard deviation SD over three repeated experimental measurements and the significant difference of the 95% confidence level.

under visible light to form a hydroxyl radical (HO), which is known to be a highly reactive, oxidizing agent, which can damage bacterial cell walls, proteins, and nucleic acids. Ilmenite is also composed of Fe and produces the above-mentioned radicals under visible light. These hydroxyls and peroxy radical compounds react with the microorganism and can damage the cell wall, so that cells will leak (see Figure 6). The cytoplasm of cells will experience dryness, resulting in the death of microorganisms. The magnitude of the light-induced cellular destruction and extent of cell density reduction are higher in the cal-Ilm/GO nanohybrid. GO is a material with a high surface area, and it enhances the photocatalytic activity of ilmenite. This may be the reason for the increased antimicrobial activity of the cal-Ilm/GO nanohybrid compared to the cal-Ilm. According to these quantitative results, the prepared cal-Ilm/GO nanohybrid will provide a potential and beneficial way for the destruction of *Escherichia coli*.

3.3. Shelf Life Studies of Alginate/Cal-Ilm/GO Nanohybrid-Coated Bananas with Physicochemical Parameters.

The activity of the alginate/cal-Ilm/GO nanohybrid films was further confirmed via a banana fruit ripening test. The novel alginate/cal-Ilm/GO nanohybrid and three control coating solutions were tested on bananas. The bananas were exposed to constant light over the entire period of storage. Weight loss and firmness changes were observed regularly on each tested date regularly. Bananas are typically harvested when they are still unripe (green) and remain this way until they mature, maintaining their green color and firmness. During the maturation period, flavor developed, and the fruit appeared softened. Banana is prone to chemical and physical deterioration easily during storage, and due to the quick ripening process, the surface becomes dark. Reportedly, the formation of a brown pigment was because of polyphenol oxidase, which changes phenol to quinone, and polymerization, resulting in the increase in macromolecules. Initially, ripeness is assessed visually by comparing the appearance of the banana with and without coating up to 12 days (see Figure 8). All bananas initially exhibited a green-yellow color and an unblemished surface. However, they are prone to decay with
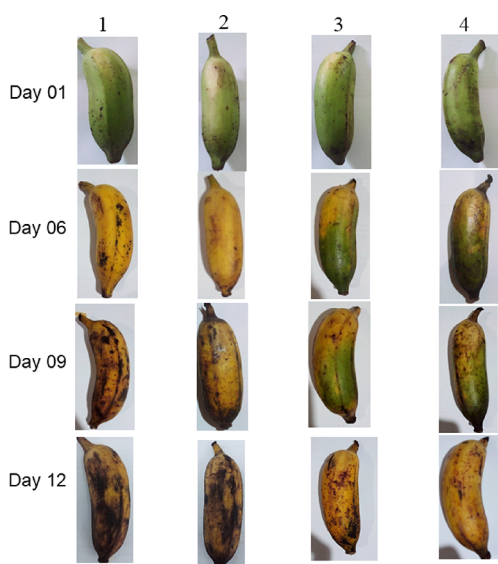

Figure 8. Images of the bananas (1) water-dipped, (2) alginate-coated, (3) alginate/cal-Ilm-coated, and (4) alginate/cal-Ilm/GO nanohybrid-coated.

increasing storage periods, as evidenced by the formation of black spots and brown pigments on the surface. The natural green color of the bananas faded considerably into yellow in uncoated bananas. During postharvest storage, control banana samples (water-dipped and alginate solution-coated bananas) developed a yellow color in the peel on the sixth day, and the color changes increased fast. According to the one-way ANOVA, the uncoated sample and the alginate cal-lm/GO-coated banana on the sixth day showed a significant difference in both broad methane and sulfur alcohol. On the 12th day, control banana samples developed brown spots and lost their commercial value: thus, the experiment was stopped. However, the alginate/cal-Ilm/GO-coated bananas were fresh compared with the control samples. It was visible that the alginate/cal-Ilm/GO nanohybrid coating provides better preservation for the bananas.

Typical changes in the physicochemical properties in bananas were reported by using the weight loss, firmness, and electronic nose measurements. The weight of a banana tends to decrease with storage because it is a perishable fruit regardless of the care that was taken to preserve it. Weight loss is used as an indicator of the freshness of agricultural products. The two most important reasons for reducing the weight loss of fruits and vegetables are transpiration water loss and reserved carbon loss. It was observed that the weight loss of the alginate/cal-Ilm/GO nanohybrid was less than 0.10% after 12 days of storage. However, all of the other control banana samples showed weight loss percentages higher than 0.10%. Therefore, the weight loss of bananas is lower in alginate/ilmenite/GO-coated bananas compared to others. The softening of the banana fruit is associated with a degradation of cell wall compounds, a reduction of starch, and an increase in the sugar content. A decrease in firmness is considered one of the most direct characteristics that change during fruit ripening, and it has a relation with food development and ripening. The firmness of the control bananas (water-dipped and alginate solution-coated bananas) also declined sharply, but the firmness in bananas covered with the alginate/cal-Ilm/GO nanohybrid was much higher. This rapid softening corresponds to the alteration of the pectic substances. These results demonstrated that the alginate/cal-Ilm/GO nanohybrid coating delayed the fruit ripening by enhancing the fruit preservation. Electronic nose testing was also carried out to confirm the efficiency of the prepared alginate/cal-Ilm/GO nanohybrid in fruit preservation. Fruits produce several volatile organic molecules at varying concentrations as they mature. Off flavor developed within a short period of time due to the higher ethanol and ethyl acetate in the fruit. There are higher aldehydes, ketones, and alcohols at the 12th day in control banana samples, which leads to off flavor following the reduction of the quality of bananas. Therefore, it can be mentioned that the shelf life of bananas developed up to 12 days by alginate/cal-Ilm/GO nanohybrid-coated bananas as shown in Figure 9. There are similar results reported about the extension of the shelf life of bananas with the TiO$_2$-based coating and packaging films,[62,63] such as those of Ezati et al. who conducted research on CuO-doped titanium dioxide nanotubes for active food packaging applications.[11,12]

4. CONCLUSIONS

The utilization of photocatalytic activity of an ilmenite-based photocatalyst to reduce the postharvest losses is studied. A highly effective ilmenite nanohybrid incorporating GO was
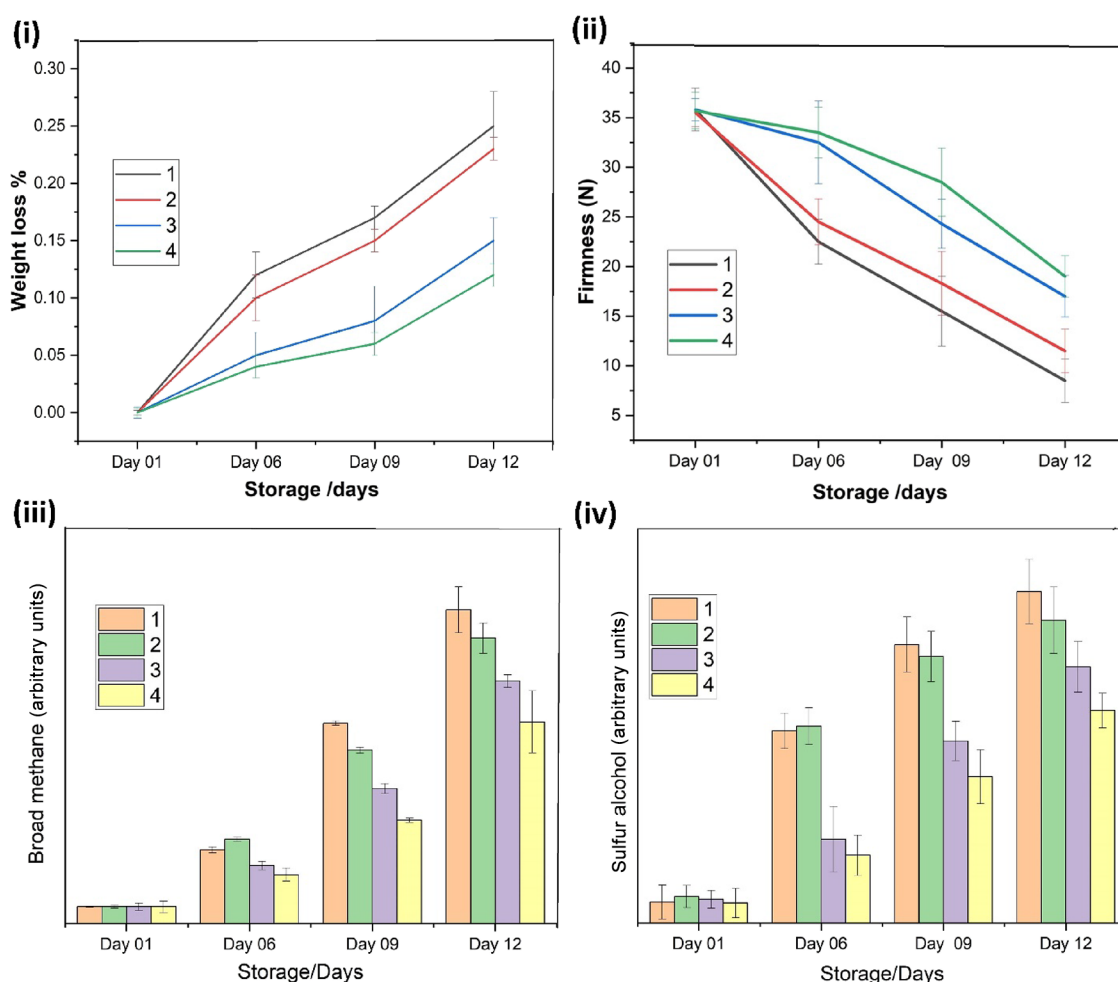
Figure 9. Effect of the fruit coatings on the (i) weight loss, (ii) firmness changes, (iii) broad methane, and (iv) alcohol changes of (1) uncoated, (2) alginate-coated, (3) alginate/cal-Ilm, and (4) alginate/cal-Ilm/GO nanohybrid. Each column represents means ± SD over three repeated experimental measurements.

successfully synthesized using a facile microwave-assisted method at a relatively low temperature of 140 °C and a brief duration of 7 min. While ilmenite alone exhibited modest *Escherichia coli* inactivation efficiency, the introduction of GO in the cal-Ilm/GO nanohybrid significantly enhanced the bactericidal efficacy. Moreover, the alginate/cal-Ilm/GO nanohybrid-coated bananas exhibited a prolonged shelf life. Additionally, assessment of the physicochemical properties using weight loss, firmness, and electronic nose measurements indicated less deterioration in the nanohybrid-coated bananas. While the cytocompatibility of the coating remains to be studied, this innovative approach is expected to expand the range of applications for natural ilmenite in photocatalysis, offering a novel ilmenite-mediated photocatalytic strategy for microbial control.

ASSOCIATED CONTENT

Supporting Information

The Supporting Information is available free of charge at https://pubs.acs.org/doi/10.1021/acsomega.4c03231.

Chemical composition of beach sand; EDX patterns and XPS survey spectra of natural ilmenite, cal-Ilm, and cal-Ilm/GO; SAED pattern of cal-Ilm/GO (PDF)

AUTHOR INFORMATION

Corresponding Authors

Dilushan Jayasundara − *Department of Physics, University of Colombo, Colombo 003000, Sri Lanka;* orcid.org/0000-0001-9220-1130; Phone: 0094 770895369; Email: dilushanj@phys.cmb.ac.lk

Nilwala Kottegoda − *Department of Chemistry, Faculty of Applied Sciences, University of Sri Jayewardenepura, Nugegoda 10250, Sri Lanka;* orcid.org/0000-0002-9664-1704; Phone: 0094 2804206; Email: nilwala@sjp.ac.lk

Authors

Piyumi Kodithuwakku − *Department of Chemistry, Faculty of Applied Sciences, University of Sri Jayewardenepura, Nugegoda 10250, Sri Lanka*

Imalka Munaweera − *Department of Chemistry, Faculty of Applied Sciences and Instrument Center, Faculty of Applied Sciences, University of Sri Jayewardenepura, Nugegoda 10250, Sri Lanka;* orcid.org/0000-0002-0665-1563

Randika Jayasinghe − *Department of Civil and Environmental Technology, Faculty of Technology, University of Sri Jayewardenepura, Nugegoda 10100, Sri Lanka*

Tharanga Thoradeniya — *Department of Biochemistry and Molecular Biology, Faculty of Medicine, University of Colombo, Colombo 003000, Sri Lanka*

Achala Bogahawatta — *Department of Microbiology, Faculty of Medical Sciences, University of Sri Jayewardenepura, Nugegoda 10250, Sri Lanka*

K. R. Jaliya Manuda — *Department of Physics, University of Colombo, Colombo 003000, Sri Lanka;* ⊙ orcid.org/0000-0002-3333-6649

Manjula Weerasekera — *Department of Microbiology, Faculty of Medical Sciences, University of Sri Jayewardenepura, Nugegoda 10250, Sri Lanka*

Complete contact information is available at:
https://pubs.acs.org/10.1021/acsomega.4c03231

Notes
The authors declare no competing financial interest.

■ **REFERENCES**

(1) Kumari, C.; Sharma, M.; Kumar, V.; Sharma, R.; Kumar, V.; Sharma, P.; Kumar, P.; Irfan, M. Genome Editing Technology for Genetic Amelioration of Fruits and Vegetables for Alleviating Post-Harvest Loss. *Bioengineering* **2022**, *9* (4), 176.

(2) Arora, N. K.; Mishra, I. Current Scenario and Future Directions for Sustainable Development Goal 2: A Roadmap to Zero Hunger. *Environ. Sustain.* **2022**, *5* (2), 129−133.

(3) Wan, C.; Kahramanoğlu, İ.; Chen, J.; Gan, Z.; Chen, C. Effects of Hot Air Treatments on Postharvest Storage of Newhall Navel Orange. *Plants* **2020**, *9* (2), 170.

(4) Revynthi, A. M.; Peña, J. E.; Moreno, J. M.; Beam, A. L.; Mannion, C.; Bailey, W. D.; Carrillo, D. Effectiveness of Hot-Water Immersion Against Brevipalpus Yothersi (Acari: Tenuipalpidae) as a Postharvest Treatment for Lemons. *J. Econ. Entomol.* **2019**, *113* (1), 126−133.

(5) Liu, W.; Zhang, M.; Bhandari, B. Nanotechnology − A Shelf Life Extension Strategy for Fruits and Vegetables. *Crit. Rev. Food Sci. Nutr.* **2020**, *60* (10), 1706−1721.

(6) Maresca, D.; Mauriello, G. Development of Antimicrobial Cellulose Nanofiber-Based Films Activated with Nisin for Food Packaging Applications. *Foods* **2022**, *11* (19), 3051.

(7) Khalil, H. A.; Abdelkader, M. F. M.; Lo'ay, A. A.; El-Ansary, D. O.; Shaaban, F. K. M.; Osman, S. O.; Shenawy, I. E.; Osman, H. E. H.; Limam, S. A.; Abdein, M. A.; Abdelgawad, Z. A. The Combined Effect of Hot Water Treatment and Chitosan Coating on Mango (Mangifera Indica L. Cv. Kent) Fruits to Control Postharvest Deterioration and Increase Fruit Quality. *Coatings 2022, Vol. 12, Page 83* **2022**, *12* (1), 83.

(8) Munhuweyi, K.; Mpai, S.; Sivakumar, D. Extension of Avocado Fruit Postharvest Quality Using Non-Chemical Treatments. *Agronomy* **2020**, *10* (2), 212.

(9) Wassermann, B.; Kusstatscher, P.; Berg, G. Microbiome Response to Hot Water Treatment and Potential Synergy With Biological Control on Stored Apples. *Front. Microbiol.* **2019**, *10*, 490265.

(10) Oyom, W.; Li, Y.-c.; Prusky, D.; Zhang, Z.; Bi, Y.; Tahergorabi, R. Recent Advances in Postharvest Technology of Asia Pears Fungi Disease Control: A Review. *Physiol. Mol. Plant Pathol.* **2022**, *117*, No. 101771.

(11) Ezati, P.; Riahi, Z.; Rhim, J. W. CMC-Based Functional Film Incorporated with Copper-Doped TiO2 to Prevent Banana Browning. *Food Hydrocoll.* **2022**, *122*, No. 107104.

(12) Ezati, P.; Riahi, Z.; Rhim, J.-W. Carrageenan-Based Functional Films Integrated with CuO-Doped Titanium Nanotubes for Active Food-Packaging Applications. *ACS Sustain. Chem. Eng.* **2021**, *9* (28), 9300−9307.

(13) Zhang, W.; Sani, M. A.; Zhang, Z.; McClements, D. J.; Jafari, S. M. High Performance Biopolymeric Packaging Films Containing Zinc Oxide Nanoparticles for Fresh Food Preservation: A Review. *Int. J. Biol. Macromol.* **2023**, *230*, No. 123188.

(14) Akshaykranth, A.; Jayarambabu, N.; Venkatappa Rao, T.; Rakesh Kumar, R.; Srinivasa Rao, L. Antibacterial Activity Study of ZnO Incorporated Biodegradable Poly (Lactic Acid) Films for Food Packaging Applications. *Polym. Bull.* **2023**, *80* (2), 1369−1384.

(15) Kodithuwakku, P.; Jayasundara, D. R.; Munaweera, I.; Jayasinghe, R.; Thoradeniya, T.; Weerasekera, M.; Ajayan, P. M.; Kottegoda, N. A Review on Recent Developments in Structural Modification of TiO2 for Food Packaging Applications. *Prog. Solid State Chem.* **2022**, *67*, No. 100369.

(16) Panariello, L.; Coltelli, M. B.; Hadrich, A.; Braca, F.; Fiori, S.; Haviv, A.; Miketa, F.; Lazzeri, A.; Staebler, A.; Gigante, V.; Cinelli, P. Antimicrobial and Gas Barrier Crustaceans and Fungal Chitin-Based Coatings on Biodegradable Bioplastic Films. *Polymers (Basel).* **2022**, *14* (23), 5211.

(17) Xu, H.; Ke, L.; Tang, M.; Shang, H.; Xu, W.; Zhang, Z.; Fu, Y.; Han, G.; Cui, J.; Yang, H.; Gao, J.; Zhang, S.; He, X. In-situ Liquid Exfoliation of Montmorillonite Nanosheets in Poly(lactic Acid)to Resist Oxygen Permeation. *Chem. J. Chin. Univ.* **2022**, *43* (11), 1−9.

(18) Olawore, O.; Ogunmola, M.; Desai, S. Engineered Nanomaterial Coatings for Food Packaging: Design, Manufacturing, Regulatory, and Sustainability Implications. *Micromachines* **2024**, *15* (2), 245.

(19) Vieira, I. R. S.; de Carvalho, A. P. A. de; Conte-Junior, C. A. Recent Advances in Biobased and Biodegradable Polymer Nanocomposites, Nanoparticles, and Natural Antioxidants for Antibacterial and Antioxidant Food Packaging Applications. *Compr. Rev. Food Sci. Food Saf.* **2022**, *21* (4), 3673−3716.

(20) Suvarna, V.; Nair, A.; Mallya, R.; Khan, T.; Omri, A. Antimicrobial Nanomaterials for Food Packaging. *Antibiotics* **2022**, *11* (6), 729.

(21) Chawla, R.; Sivakumar, S.; Kaur, H. Antimicrobial Edible Films in Food Packaging: Current Scenario and Recent Nanotechnological Advancements- a Review. *Carbohydr. Polym. Technol. Appl.* **2021**, *2*, No. 100024.

(22) Seneviratne, K. L.; Munaweera, I.; Peiris, S. E.; Kodithuwakku, P.; Peiris, C. N.; Kottegoda, N. Visible Light Active Silver Decorated Iron Titanate/Titanium Dioxide Nanohybrid for Sterilization of Explants Grown by In Vitro Technique. *Adv. Mater. Technol.* **2023**, *8* (6), 2201292.

(23) Nguyen, S. V.; Lee, B.-K. Multifunctional Nanocomposite Based on Polyvinyl Alcohol, Cellulose Nanocrystals, Titanium Dioxide, and Apple Peel Extract for Food Packaging. *Int. J. Biol. Macromol.* **2023**, *227*, 551−563.

(24) Priyadarshi, R.; Negi, Y. S. Effect of Varying Filler Concentration on Zinc Oxide Nanoparticle Embedded Chitosan Films as Potential Food Packaging Material. *J. Polym. Environ.* **2017**, *25* (4), 1087−1098.

(25) Mei, L.; Wang, Q. Advances in Using Nanotechnology Structuring Approaches for Improving Food Packaging. In *Annual Review of Food Science and Technology*; Annual Reviews, 2020; Vol. 11, pp 339−364. DOI: 10.1146/ANNUREV-FOOD-032519-051804.

(26) Agarwal, H.; Menon, S.; Venkat Kumar, S.; Rajeshkumar, S. Mechanistic Study on Antibacterial Action of Zinc Oxide Nanoparticles Synthesized Using Green Route. *Chem. Biol. Interact.* **2018**, *286*, 60−70.

(27) Mihaly Cozmuta, A.; Peter, A.; Mihaly Cozmuta, L.; Nicula, C.; Crisan, L.; Baia, L.; Turila, A. Active Packaging System Based on Ag/TiO2 Nanocomposite Used for Extending the Shelf Life of Bread. Chemical and Microbiological Investigations. *Packag. Technol. Sci.* **2015**, *28* (4), 271−284.

(28) El-Shafai, N.; El-Khouly, M. E.; El-Kemary, M.; Ramadan, M.; Eldesoukey, I.; Masoud, M. Graphene Oxide Decorated with Zinc Oxide Nanoflower, Silver and Titanium Dioxide Nanoparticles: Fabrication, Characterization, DNA Interaction, and Antibacterial Activity. *RSC Adv.* **2019**, *9* (7), 3704−3714.

(29) Afzal, M. J.; Pervaiz, E.; Farrukh, S.; Ahmed, T.; Bingxue, Z.; Yang, M. Highly Integrated Nanocomposites of RGO/TiO2 Nanotubes for Enhanced Removal of Microbes from Water. *Environ. Technol.* **2019**, *40* (19), 2567−2576.

(30) Premaratne, W. A. P. J.; Rowson, N. A. Microwave Assisted Dissolution of Sri Lankan Ilmenite: Extraction and Leaching Kinetics of Titanium and Iron Metals. *J. Sci. Univ. Kelaniya* **2015**, *9* (0), 01−14.

(31) Gu, D.; Qin, Y.; Wen, Y.; Qin, L.; Seo, H. J. Photochemical and Magnetic Activities of FeTiO3 Nanoparticles by Electro-Spinning Synthesis. *J. Taiwan Inst. Chem. Eng.* **2017**, *78*, 431−437.

(32) Moradi, M.; Vasseghian, Y.; Khataee, A.; Harati, M.; Arfaeinia, H. Ultrasound-assisted Synthesis of FeTiO3/GO Nanocomposite for Photocatalytic Degradation of Phenol under Visible Light Irradiation. *Sep. Purif. Technol.* **2021**, *261*, No. 118274.

(33) Cañas-Martínez, D. M.; Gauthier, G. H.; Pedraza-Avella, J. A. Photo-Oxidative and Photo-Reductive Capabilities of Ilmenite-Rich Black Sand Concentrates Using Methyl Orange as a Probe Molecule. *Photochem. Photobiol. Sci.* **2019**, *18* (4), 912−919.

(34) Chen, Y.-H.; Li, F.-A. Nano-Ilmenite with Dual Functions of Photocatalysis and Adsorption. *J. Miner. Met. Mater. Soc.* **2018**, *70* (10), 1924−1928.

(35) Wang, H.; Li, X.; Zhao, X.; Li, C.; Song, X.; Zhang, P.; Huo, P.; Li, X. A Review on Heterogeneous Photocatalysis for Environmental Remediation: From Semiconductors to Modification Strategies. *Chin. J. Catal.* **2022**, *43* (2), 178−214.

(36) Chen, Y. H. Synthesis, Characterization and Dye Adsorption of Ilmenite Nanoparticles. *J. Non. Cryst. Solids* **2011**, *357* (1), 136−139.

(37) Tang, X.; Hu, K. The Formation of Ilmenite FeTiO3 Powders by a Novel Liquid Mix and H2/H2O Reduction Process. *J. Mater. Sci.* **2006**, *41* (23), 8025−8028.

(38) Sunkara, S. S.; Pandey, R. K. Ilmenite−a Wide Bandgap Semiconductor for Novel Electronic Applications. *Ceram. Trans.* **1995**, *60*, 83−93.

(39) Robinson, P.; Harrison, R. J.; McEnroe, S. A.; Hargraves, R. B. Lamellar Magnetism in the Haematite−Ilmenite Series as an Explanation for Strong Remanent Magnetization. *Nature* **2002**, *418* (6897), 517−520.

(40) Wilson, N. C.; Muscat, J.; Mkhonto, D.; Ngoepe, P. E.; Harrison, N. M. Structure and Properties of Ilmenite from First Principles. *Phys. Rev. B* **2005**, *71* (7), No. 075202.

(41) Mehdilo, A.; Irannajad, M.; Rezai, B. Chemical and Mineralogical Composition of Ilmenite: Effects on Physical and Surface Properties. *Miner. Eng.* **2015**, *70*, 64−76.

(42) Wang, R.; Shi, M.; Xu, F.; Qiu, Y.; Zhang, P.; Shen, K.; Zhao, Q.; Yu, J.; Zhang, Y. Graphdiyne-Modified TiO2 Nanofibers with Osteoinductive and Enhanced Photocatalytic Antibacterial Activities to Prevent Implant Infection. *Nat. Commun.* **2020**, *11* (1), 1−12.

(43) Yu, W.; Sisi, L.; Haiyan, Y.; Jie, L. Progress in the Functional Modification of Graphene/Graphene Oxide: A Review. *RSC Adv.* **2020**, *10* (26), 15328−15345.

(44) Joshi, S.; Bobade, H.; Sharma, R.; Sharma, S. Graphene Derivatives: Properties and Potential Food Applications. *J. Ind. Eng. Chem.* **2023**, *123*, 1−18.

(45) Han Lyn, F.; Nur Hanani, Z. A. Graphene-Based Polymer Nanocomposites in Food Packaging and Factors Affecting the Behaviour of Graphene-Based Materials: A Review. *J. Nanoparticle Res.* **2022**, *24* (9), 1−21.

(46) Ali, M.; Hussain, R.; Tariq, F.; Noreen, Z.; Toufiq, A. M.; Bokhari, H.; Akhtar, N.; ur Rahman, S. Highly Effective Visible Light-Activated Cobalt-Doped TiO2 Nanoparticles for Antibacterial Coatings against Campylobacter Jejuni. *Appl. Nanosci.* **2020**, *10* (3), 1005−1012.

(47) Giovannetti, R.; Rommozzi, E.; Zannotti, M. I.; D'Amato, A. C. Recent Advances in Graphene Based TiO2 Nanocomposites (GTiO2Ns) for Photocatalytic Degradation of Synthetic Dyes. *Catalysts* **2017**, *7* (10), 305.

(48) Fatima, S.; Rizwan, S. Synergetic Catalytic and Photocatalytic Performances of Tin-Doped BiFeO3/Graphene Nanoplatelet Hybrids under Dark and Light Conditions. *ACS Omega* **2023**, *8* (4), 3736−3744.

(49) Nissanka, B.; Kottegoda, N.; Jayasundara, D. R. Probing Structural Variations of Graphene Oxide and Reduced Graphene Oxide Using Methylene Blue Adsorption Method. *J. Mater. Sci.* **2020**, *55* (5), 1996−2005.

(50) Xing, M.; Sun, K.; Liu, Q.; Pan, L.; Tu, K. Development of Novel Electronic Nose Applied for Strawberry Freshness Detection during Storage. *Int. J. Food Eng.* **2018**, *14*, 20180111.

(51) Liew, C. Y.; Lau, C. Y. Determination of Quality Parameters in Cavendish Banana during Ripening by NIR Spectroscopy. *Int. Food Res. J.* **2012**, *19* (2), 751−758.

(52) Premaratne, W. A. P. J.; Rowson, N. A. The European Journal of Mineral Processing and Environmental Protection. *Eur. J. Miner. Process. Environ. Prot.* **2004**, *4* (3), 183−193.

(53) Zarazúa-Morín, M. E.; Torres-Martínez, L. M.; Moctezuma, E.; Juárez-Ramírez, I.; Zermeño, B. B. Synthesis, Characterization, and Catalytic Activity of FeTiO3/TiO2 for Photodegradation of Organic Pollutants with Visible Light. *Res. Chem. Intermed.* **2016**, *42* (2), 1029−1043.

(54) Perera, S. D.; Mariano, R. G.; Vu, K.; Nour, N.; Seitz, O.; Chabal, Y.; Balkus, K. J. Hydrothermal Synthesis of Graphene-TiO 2 Nanotube Composites with Enhanced Photocatalytic Activity. *ACS Catal.* **2012**, *2* (6), 949−956.

(55) Wu, X.; Qin, S.; Dubrovinsky, L. Investigation into High-Pressure Behavior of MnTiO3: X-Ray Diffraction and Raman Spectroscopy with Diamond Anvil Cells. *Geosci. Front.* **2011**, *2* (1), 107−114.

(56) Rong, X.; Qiu, F.; Zhang, C.; Fu, L.; Wang, Y.; Yang, D. Preparation, Characterization and Photocatalytic Application of TiO2−Graphene Photocatalyst under Visible Light Irradiation. *Ceram. Int.* **2015**, *41* (2), 2502−2511.

(57) Wu, H.; Fan, J.; Liu, E.; Hu, X.; Ma, Y.; Fan, X.; Li, Y.; Tang, C. Facile Hydrothermal Synthesis of TiO2 Nanospindles-Reduced Graphene Oxide Composite with a Enhanced Photocatalytic Activity. *J. Alloys Compd.* **2015**, *623*, 298−303.

(58) Vo, N. Q. D.; Huynh, N. D. T.; Le, M. V.; Vo, K. D.; Vo, D. V. N. Fabrication of Ag-Photodeposited TiO2/Cordierite Honeycomb Monolith Photoreactors for 2-Naphthol Degradation. *J. Chem. Technol. Biotechnol.* **2020**, *95* (10), 2628−2637.

(59) Yalçin, Y.; Kiliç, M.; Çinar, Z. Fe+3-Doped TiO2: A Combined Experimental and Computational Approach to the Evaluation of Visible Light Activity. *Appl. Catal. B Environ.* **2010**, *99* (3−4), 469−477.

(60) Nurdin, M.; Yanti, N. A.; Suciani; Watoni, A. H.; Maulidiyah; Aladin, A.; Wibowo, D. Efficiency of Ilmenite Photocatalyst Material as Modelling for Antimicrobial Activity. *Asian J. Chem.* **2018**, *30* (6), 1387−1392.

(61) Sun, W.; Wu, F.-G. Two-Dimensional Materials for Antimicrobial Applications: Graphene Materials and Beyond. *Chem. - Asian J.* **2018**, *13* (22), 3378−3410.

(62) Xie, J.; Wang, R.; Li, Y.; Ni, Z.; Situ, W.; Ye, S.; Song, X. A Novel Ag2O-TiO2-Bi2WO6/Polyvinyl Alcohol Composite Film with Ethylene Photocatalytic Degradation Performance towards Banana Preservation. *Food Chem.* **2022**, *375*, No. 131708.

(63) Xu, J.; Wang, F.; Zhan, J.; Li, Y.; Wang, T.; Ma, R.; Tian, Y. Construction of TiO2/Starch Nanocomposite Cryogel for Ethylene

Removal and Banana Preservation. *Carbohydr. Polym.* **2023**, *312*, No. 120825.